2. Lattice: body centred cubic; $\frac{\beta^2}{\alpha^2+\beta^2}=0{\cdot}65\pm0{\cdot}1$, $\frac{\alpha}{\beta}\sim0{\cdot}7\pm0{\cdot}1$.

Hence the next neighbours (bricks) are placed along body diagonals. The fluctuation is less parallel to their mean coordination vector (20 XU) and greater at right angles to it (28 XU). ($\alpha<\beta$, see Fig. 2). It is known, that in a spinel oxygen ions build up a close packed f.c.c. lattice; the small spaces at tetragonal and octahedral sites between these large anions are filled up by the small cations. In the manganese-rich spinels under consideration obviously the cations in octahedral positions make 'bricks' with the surrounding oxygen ions and these molecular bricks themselves make up the crystalline lattice.

In another paper* the results from these spinels are dealt with in detail. The aim of the present paper is to illustrate that information relevant to the concept of paracrystals is available from line profile analysis.

* Červinka, Hosemann & Vogel (1970).

The authors wish to thank the Deutsche Forschungsgemeinschaft and the Senat von Berlin for supporting this work from the ERP funds.

References

ČERVINKA, L., HOSEMANN, R. & VOGEL, W. (1970). *Acta Cryst.* A**26**, 277.

DEBYE, P. P. (1927). *Z. Phys.* **28**, 135.

EWALD, P. P. (1940). *Proc. Phys. Soc.* **52**, 167.

HOSEMANN, R. (1950*a*). *Z. Phys.* **128**, 1, 465.

HOSEMANN, R. (1950*b*). *Acta Cryst.* **4**, 520.

HOSEMANN, R. & BAGCHI, S. N. (1952). *Acta Cryst.* **5**, 612.

HOSEMANN, R. & BAGCHI, S. N. (1962). *Direct Analysis of Diffraction by Matter*. Amsterdam: North Holland.

HOSEMANN, R., BALTA-CALLEJA, F. J. & WILKE, W. (1966). *Makromol. Chem.* **92**, 25.

HOSEMANN, R., PREISINGER, A. & VOGEL, W. (1966). *Ber. Bunsenges. Phys. Chem.* **70** (6), 796.

ORNSTEIN, L. S. & ZERNICKE, F. (1918). *Z. Phys.* **29**, 134.

VOGEL, W. (1967). *Gitterstörungen erster und zweiter Art in binären Legierungen und komplexen Metallverbindungen*, Diploma F.U. Berlin-Dahlem.

ZERNIKE, F. & PRINS, J. A. (1927). *Z. Phys.* **41**, 184.

Acta Cryst. (1970). A**26**, 277

Paracrystalline Lattice Distortions and Microdomains in Manganese Ferrites near the Cubic-to-Tetragonal Transition

BY L. ČERVINKA

Institute of Solid State Physics, Czech. Acad. of Sciences, Prague, Czechoslovakia

AND R. HOSEMANN AND W. VOGEL

Fritz-Haber-Institut der Max-Planck-Gesellschaft, Berlin-Dahlem, Germany

(*Received* 3 *March* 1969)

The line profiles of X-ray reflexions from different $Mn_xFe_{3-x}O_4$ samples were investigated. Sample I ($x=1{\cdot}66$) is cubic with no anomalies; small paracrystalline distortions, $g<0{\cdot}1\%$, cannot be excluded and are calculated to be of this magnitude from considerations of a simple volume effect of the larger Mn^{3+} ions. Samples II–IV ($x=1{\cdot}88$) show interesting effects which are closely connected with the development of the tetragonal structure, observed when $x>1{\cdot}80$. Sample II (quenched) shows paracrystalline distortions which can be quantitatively explained on the basis of the Jahn–Teller effect: the tetragonally deformed single $Mn^{3+}O_6^{2-}$ octahedra are statistically oriented and statistically distributed over B sites and have a mean tetragonality $\bar{\epsilon}=0{\cdot}014$. In sample III (cooling rate 20 °C.min^{-1}) about 26% of the volume consists of microdomains which result from a correlation between the orientations and positions of Jahn–Teller octahedra; quantitative agreement with the theory can be obtained by introducing a correlation factor $\gamma=2$. In sample IV (cooling rate 7 °C.min^{-1}) this correlation proceeded in such a way that the crystal consisted of 74% tetragonal matrix which had already attained a value of $c/a=1{\cdot}056$, and about 22% of tetragonal microdomains oriented in two other directions with a value $c/a<1{\cdot}056$. In addition about 3 to 5% of a cubic phase is present. If the mean tetragonality of the microdomains is taken to be $\bar{\epsilon}=0{\cdot}020$ the experiments correspond quantitatively with the theory. The detailed study of sample III proves that $H_{\frac{1}{2}\frac{1}{2}\frac{1}{2}}$ are the paracrystalline coordination statistics with a fluctuation $\alpha=27$ XU in the direction [111] and $\beta=38$ XU perpendicular to it. This is explained by a model of the spinel structure having two kinds of blocks: a tetrahedral A-structure and Jahn–Teller affected octahedral subcubes at B sites; the separation distance is $\frac{1}{4}\sqrt{3}a=3{\cdot}7$ Å.

1. Introduction

It has been proved that tetragonally distorted octahedra of $Mn^{3+}O_6^{2-}$ exist locally in the macroscopic cubic lattice of the $Mn_xFe_{3-x}O_4$ system (Červinka, Krupička & Syneček, 1961; Červinka, 1965). This can be explained quantum mechanically by Mn^{3+} ions in an octahedral environment of O^{2-} anions. The eigen-

functions then lose their higher symmetry and the chemical binding forces in one direction (c axis) becomes less than in the others; this is the effect predicted by Jahn & Teller (1937). On increasing the concentration of these manganese ions the number of Jahn–Teller Mn^{3+} ions is also increased. At a certain concentration of these ions ($x=1{\cdot}8$–$1{\cdot}9$) the spinel structure changes from a cubic to a tetragonal lattice (Fig. 1). Such a transformation is explained by a cooperative interaction of these locally tetragonally distorted octahedra. At higher concentration of Mn^{3+} ions this leads to a long range ordering process – the cubic-to-tetragonal transition (Wickham & Croft, 1958; Wojtowicz, 1959).

It is the aim of this paper to study in more detail the phenomena occurring at this transition in order to obtain more information on the role of the Jahn–Teller ions in the lattice. This is significant for other properties of spinels also, *e.g.* the deviations from theoretical values of the Curie constant (Blasse, 1965), the anomalous behaviour of the crystallographic properties of spinels with lithium (Rogers, Germann & Arnott, 1965), the anomalous variation of the low temperature lattice constant of manganese-rich manganese ferrites (Červinka & Vetterkind, 1968), and the temperature dependences of the Seebeck voltage and the electrical conductivity (Šimša, 1967).

All these anomalies have been qualitatively explained by the formation of 'clusters' of Mn^{3+} ions in the octahedral sites of the spinel lattice. Furthermore it has been pointed out that spontaneous square hysteresis loops in ferrites containing manganese could also be caused by 'clusters' of Mn^{3+} ions acting as a sort of chemical inhomogeneity in the lattice (Goodenough, 1965). To obtain more qualitative data on the clusters and microdomains (see below) we study quantitatively in this paper paracrystalline distortions of manganese-rich spinels. These distortions must occur if single Jahn–Teller ions, or clusters of them, or tetragonal microdomains exist within a cubic matrix. The mathematical background of the analysis of line widths by paracrystalline distortions is given in the preceding paper (Vogel & Hosemann, 1970).

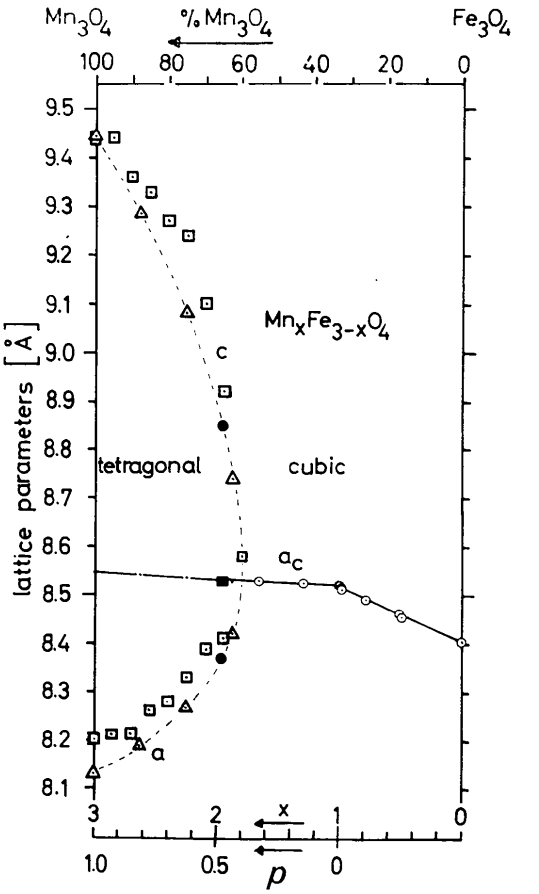

Fig. 1. Lattice parameters *versus* composition of $Mn_xFe_{3-x}O_4$ at 20°C. △ Finch, Sinha & Sinha (1967); □ McMurdie, Sullivan & Maurer (1950); ○ Červinka (1966); ● Our measurements.

2. Some crystallographic aspects

In Fig. 2 the ideal structure of a spinel below the transition point is given along an (110) netplane. A lattice cell (cell edge $a=8{\cdot}53$ Å) contains 8 f.c.c. cells of O^{2-} anions, *i.e.* 32 anions (white balls). Within the 8·53 Å lattice cell there exist 8 tetrahedral cation positions, the so called A sites (black squares) and 16 octahedral positions (black balls), the B sites. The ionic bonds are marked by lines connecting A and B site cations with anions.

In Fig. 3 the 8·53 Å lattice cell, shown by dotted lines, surrounds the 2·13 Å subcubes in such a way that a three-dimensional chessboard-like structure arises. The spinel structure can now be clearly understood:

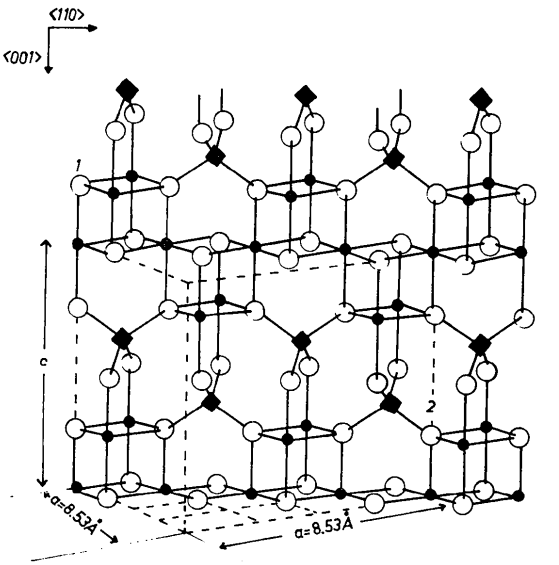

Fig. 2. Spinel structure along the (110) netplane. ○ O^{2-} ions; ● octahedral (B) cation sites; ◆ tetrahedral (A) cation sites.

one kind of subcube with 4 O^{2-} and 4 Mn^{3+} ions at the corners builds up a diamond-like 8·53 Å lattice cell. In the holes of this lattice another diamond-like lattice cell is built, displaced by $\left(\frac{a}{2}, 0, 0\right)$, whose units consist of one Me^{2+} cation of the centre, tetrahedrally surrounded by 4 O^{2-} ions. More exactly these two lattices are of the ZnS type since the subcube at (000) is not identical with that at $\left(\frac{a}{4}\frac{a}{4}\frac{a}{4}\right)$, but is inversely symmetric. The same holds for the *A* type lattice (*cf.* the subcube at $\left(0,0,\frac{a}{2}\right)$ and $\left(\frac{a}{4}, \frac{a}{4}, \frac{3a}{4}\right)$. Fig. 3, unlike Fig. 2, has the disadvantage that most of the lines do not represent ionic binding, but some details of the structure can be better understood by it.

A study of the behaviour of $Mn_xFe_{3-x}O_4$ with variation in x shows (Fig. 1) for $0<x<1$ a remarkable increase of a with x (quasi linear). This can easily be explained by the fact that, firstly, all the tetrahedral sites are filled up with Mn^{2+} ions. Since their distance from the tetrahedral anions is $\frac{1}{2}\sqrt{3}$ times smaller than the distance of *B* site cations from the nearest anions and the radius of the Mn^{2+} ion is larger than that of the Fe^{3+} ion ($R=0{\cdot}91$ Å against $R=0{\cdot}67$ Å) at $x=1$, practically all *A* sites are filled up with Mn^{2+} ions and for $x>1$ the lattice constant increases more slowly with x (Fe^{3+} has $R=0{\cdot}67$ Å, practically the same as for Mn^{3+}).

A more detailed study shows that for $x<1$ not all Mn cations go to *A* sites, but only a fraction y, and the remainder, $x-y$, go as Mn^{2+} to *B* sites (Goodenough, 1967):

$$\underset{A\text{ sites}}{Fe^{3+}_{1-y}\,Mn^{2+}_{y}}\ \underset{B\text{ sites}}{(Fe^{2+}_{1-x}\,Fe^{3+}_{1+y}\,Mn^{2+}_{x-y})} \qquad \text{for } 0<y<x<1\,. \quad (1)$$

On the other hand, according to Goodenough, for $x\gtrsim 1$ a fraction $(x-1)$ of Mn cations go with a charge of three to *B* sites:

$$\underset{A\text{ sites}}{Fe^{3+}_{1-y}\,Mn^{2+}_{y}}\ \underset{B\text{ sites}}{(Fe^{3+}_{2-x+y}\,Mn^{2+}_{1-y}\,Mn^{3+}_{x-1})} \qquad \text{for } y<1<x<2\,. \quad (2)$$

As a first approximation we described the phenomenon by

$$\begin{aligned} y&=x && \text{if } x<1\\ y&=1 && \text{if } x>1\,. \end{aligned}$$

As seen from Fig. 1, for $x>1{\cdot}88$ the tetragonal structure exists with a c axis larger than the two a axes. Moreover, in Fig. 1 $(a^2c)^{1/3}$ is plotted in the tetragonal region and it fits with the extrapolated variation of the cubic lattice cell for $1<x<2$. This proves that the volume change after the tetragonal transition remains the same as before. Hence all Mn cations built in at $x>1{\cdot}9$ have the same charge (3+) as in the region $1<x<2$ (*cf.* equation 2). Hence in practically the whole range $1<x<3$ only Mn^{3+} ions are built in at *B* sites. The percentage, p, of available *B* sites, occupied by Mn^{3+} is therefore given by

$$p=\frac{x-1}{2}\,.\,100\,\%\,.$$

The p scale is also plotted in Fig. 1.

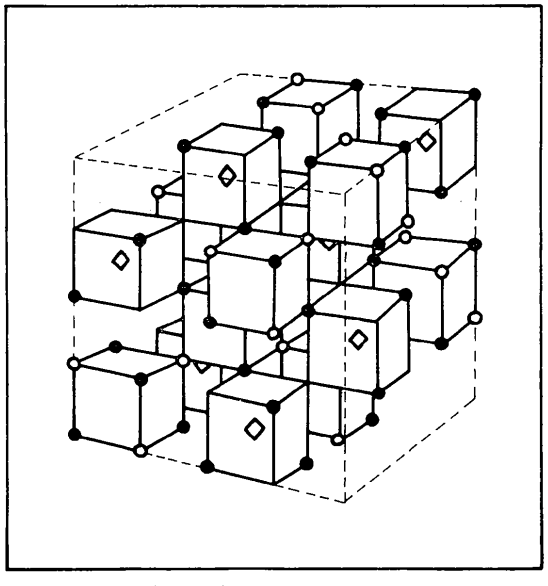

Fig. 3. The two kinds of brick of the paracrystalline b.c.c. lattice in $Mn_xFe_{3-x}O_4$ (schematic). ● O^{2-}; ◇ *A* sites; ○ *B* sites.

3. Experiments and specimen preparation

Two specimens with $x=1{\cdot}66$ and $x=1{\cdot}88$ were prepared by different methods:

(*a*) The $x=1{\cdot}66$ sample

The material was preheated to 900 °C in air and then pressed and sintered at 1230 °C for 6 hours under an atmospheric pressure of about 2 mmHg and then

Table 1. *Specimen data*

Specimen number	Manganese content, x	Amount, p, of Mn^{3+} on *B* sites	Cooling rate (°C.min^{-1})	Lattice type
I	1·66	0·33		Cubic
II	1·88	0·44	Quenched	Cubic
III	1·88	0·44	20	Pseudocubic
IV	1·88	0·44	7	Pseudotetragonal

cooled slowly from 1200°C in argon under a pressure of about 10 mm Hg (specimen I in Table 1).

(*b*) The $x=1{\cdot}88$ sample

This sample was prepared by the Verneuil method at 1580°C and cooled slowly from approximately 1200°C at a mean cooling rate of 20°C.min^{-1} (specimen III in Table 1).

Two specimens from this sample were then given a further treatment:

Specimen II (Table 1): quenched from 900°C in water.

Specimen IV (Table 1): slowly cooled from 900°C at a cooling rate of 7°C.min^{-1}.

This treatment was carried out under atmospheric conditions. Because of the long cooling time specimen IV was oxidized so that it contained 3–5% α-$(Fe, Mn)_2O_3$.

Measurements were carried out by use of a Guinier double cylinder camera, after Hofmann & Jagodzinski (1955) together with a focusing quartz crystal monochromator of the Johannson type.* Up to the 662 reflexion Fe $K\alpha_1$ radiation was used. A finest Mo-focus X-ray tube after Hosemann & Beitz* with a minimal line focus of 5μ was used for high order reflexions. The resolving power thus obtained was about 1000 Å for Mo radiation and about 1600 Å for Fe radiation (with an accuracy of 10%). With a lower accuracy of 50% the resolution reached values of 3000 and 5000 Å respectively.

* Manufactured by AEG-Telefunken.

Double coated Adox-Films were scraped off at the back after development care being taken to maintain the density S at less than $S=0{\cdot}8$.

4. Analysis of line broadening as a Jahn–Teller effect

Using the fundamental formula (15) of the preceding paper,

$$\delta b = \frac{1}{L} + \pi^2 g^2_{h_1h_2h_3}\, d_{h_1h_2h_3}\, b^2 = \frac{1}{L} + \pi^2 \frac{\Delta^2 x_a}{a^3} h^2 , \tag{3}$$

one obtains, from a $\delta b - h^2$ or $\delta b - b^2$ plot, the relative paracrystalline distance fluctuations, $g_{h_1h_2h_3}$ of a family of netplanes $h_1h_2h_3$ of mean separation $d_{h_1h_2h_3}$, or the distance fluctuation Δx_a recalculated (normalized) relative to the cell edge a, where

$$h^2 = h_1^2 + h_2^2 + h_3^2 ; \tag{4}$$

L is the weight-averaged size of the crystal normal to the netplanes, δb the observed integral width of a reflexion at $b = 2 \sin\theta/\lambda$ or at h.

Fig. 4 shows the Mo-transmission patterns of sample III compared with sample I (bottom), which show entirely sharp lines. The diffuse lines of the $x=1{\cdot}88$ sample, which become much weaker with increasing b, cannot be explained by a Debye factor alone.

In Fig. 5 the $\delta b - h$ plot of sample III is given: it shows the parabolic character of equation (3). In the

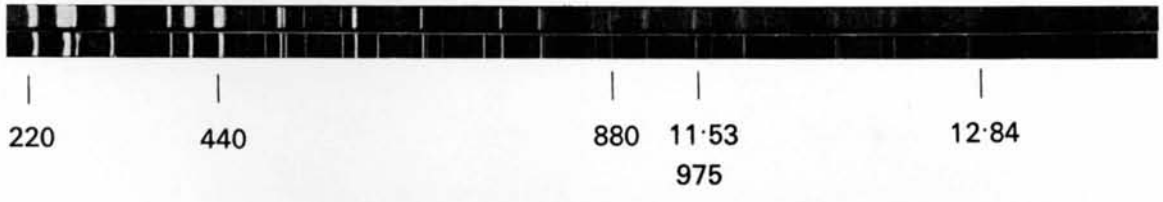

Fig. 4. Top: transmission pattern of sample III, Mo $K\alpha_2$, 50 kV, 3 mA, 185 h; bottom: transmission pattern of sample I, Mo $K\alpha_2$, 50 kV, 3 mA, 100 h.

Table 2. *Observed paracrystalline distortions along the body diagonal*

Sample	g_{111} (%)	Δx_a (XU)	L (Å)	α^*
I	$<0{\cdot}1$	<7	>6000	
II	$0{\cdot}33 \pm 0{\cdot}09$	21	4000 ± 1000	$0{\cdot}14 \pm 0{\cdot}05$
III	$0{\cdot}47 \pm 0{\cdot}07$	31	1740 ± 300	$0{\cdot}13 \pm 0{\cdot}03$
IV	$0{\cdot}69 \pm 0{\cdot}04$	45	1700 ± 300	$0{\cdot}18 \pm 0{\cdot}02$

Table 3. *Experimental results from sample* III (*pseudocubic*)

Lattice direction	g_{hkl} (%)	[*hkl*]	g_a (%)	Δx_a (XU)	L (Å)	α^*
⟨001⟩	$1{\cdot}24 \pm 0{\cdot}12$	[004]	$0{\cdot}62 \pm 0{\cdot}06$	53 ± 6	1150 ± 200	$0{\cdot}16 \pm 0{\cdot}03$
⟨011⟩	$0{\cdot}91 \pm 0{\cdot}06$	[022]	$0{\cdot}54 \pm 0{\cdot}03$	46 ± 4	1540 ± 200	$0{\cdot}17 \pm 0{\cdot}03$
⟨111⟩	$0{\cdot}47 \pm 0{\cdot}07$	[111]	$0{\cdot}36 \pm 0{\cdot}05$	31 ± 4	1740 ± 300	$0{\cdot}13 \pm 0{\cdot}03$

$\delta b - h^2$ plot of Fig. 6 on the other hand, within experimental error, linear functions can be used for all three samples II–IV. If the line broadening is explained by microstrains, the $\delta b - h$ plot of Fig. 5 must be linearly interpolated. This, within the errors of experiment, is impossible and if done yields a negative interception with the ordinate, which is meaningless.

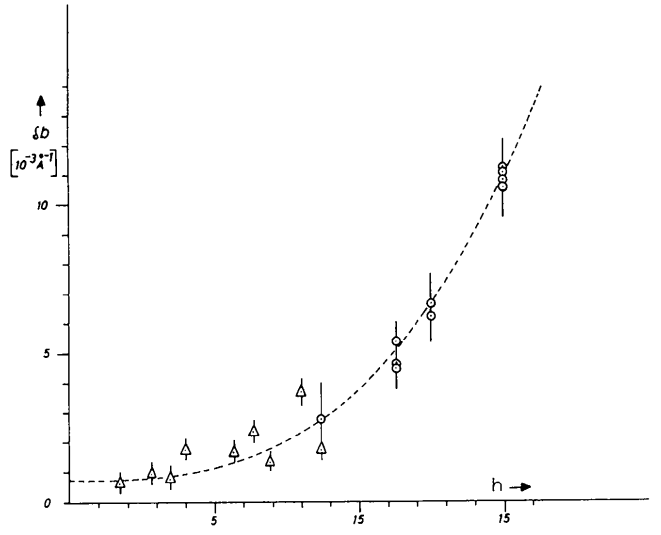

Fig. 5. Corrected integral width of sample III. Reflexions of all types are included. △ measurements with Fe $K\alpha_1$, ○ measurements with Mo $K\alpha_2$. The reflexions at $h=\sqrt{48}=6{\cdot}9$ and $h=\sqrt{75}=8{\cdot}6$ have systematically smaller widths. This is explained in Fig. 7.

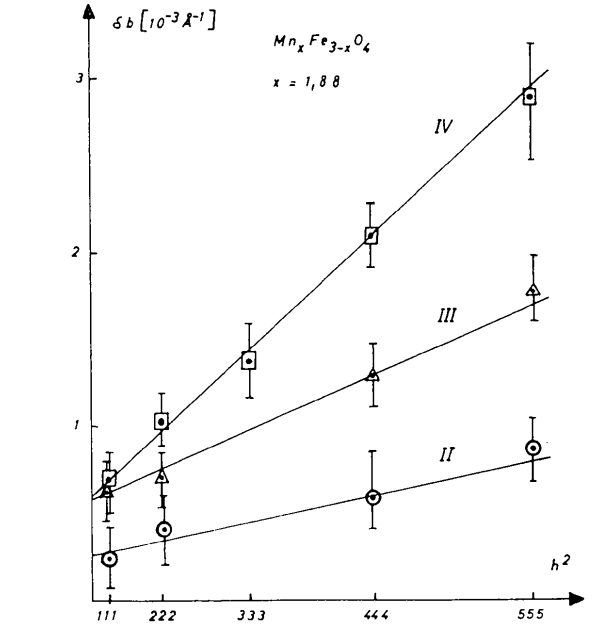

Fig. 6. Integral width, δb, of the *hhh* reflexions of samples II–IV *versus* h^2.

In Table 2 the values g_{111} for all samples and the normalized Δx_a-fluctuation are given. The quantity α^* is explained below (see § 5).

Our first result is that sample I appears to have practically no paracrystalline distortions and very large mosaic blocks, whilst the higher the number of the sample, the larger g_{111} and the smaller L. The next result is that the observed paracrystalline distortions indicate that in samples II–IV the Jahn–Teller effect plays a predominant role.

For spherical ions (radius R), the rate of change of the lattice constant a in the region $x>1$ gives, according to Vegard's rule:

$$\frac{\mathrm{d}a}{a} = p\,\frac{\mathrm{d}R}{R}\;; \tag{4}$$

$\mathrm{d}a$ is the change in the length of a cell edge a when the Fe^{3+} ion in the one B site along the cell edge a (see Fig. 2) is replaced by a Mn^{3+} ion. From Fig. 1 and published measurements (Červinka & Vetterkind, 1968) values of $a=8{\cdot}515$ and $8{\cdot}527$ Å for $p=0$ and $0{\cdot}44$ respectively, give

$$\frac{\mathrm{d}R}{R} = \frac{0{\cdot}012}{8520}\cdot\frac{1}{0{\cdot}44} = 0{\cdot}32\%\,. \tag{5}$$

The g value along this direction is then (Hosemann, Bialas, Schönfeld, Wilke & Weick, 1966)

$$g_{100} = \frac{\mathrm{d}R}{R}\sqrt{p(1-p)} = 0{\cdot}16\%\,, \tag{6}$$

and hence

$$\Delta x_a = 8{\cdot}53\times 0{\cdot}0016 = 0{\cdot}013\text{ Å} = 13\text{ XU}\,. \tag{7}$$

This value, within experimental error, may fit with sample I but is much too small compared with samples II–IV.

As proved in the preceding paper (Vogel & Hosemann, 1970), differences in the g_{hkl} values for different netplanes can be produced by specially shaped coordination statistics, for instance disc-like coordination statistics H_k in a primitive cubic lattice. Then Δx_a of [100] can be much smaller than that of [111]. Table 3, however, shows that in the direction [100] the distortions are still greater than in [111]. It is impossible that in the quenched sample II the Mn^{3+} ions group together to form clusters; we will suppose for simplicity that any such positional correlations are not important. Then the discrepancies between the Δx_a values of Table 2 and equation (7) can only be explained by a structure of octahedra deformed by Mn^{3+} ions on B sites.

5. The paracrystalline lattice cell and coordination statistics

The best data from which to determine the paracrystalline lattice cell and coordination statistics are those from sample III, since in IV some of the reflexions of the *h*00 and *hh*0 netplanes are so split or overlap to such an extent, that the results are disturbed.

Fig. 7 shows a plot of the observed widths δb *versus* h^2. Three orders of one netplane could only be obtained for (*hhh*)- and (0*hh*)-type netplanes. Reflexions 022, 044, 088 and 111, 222 and 444 are well placed on a straight line; 555 is also included. Its width is a little disturbed by the overlapping with the comparatively weak 157 reflexions. Each slope leads by means of equation (3) to a Δx_a value and these are applied to the log Δx_a *versus* $\beta^2(\alpha^2+\beta^2)^{-1}$ plot of Fig. 8. It is found directly, that the paracrystalline lattice cell must behave like a b.c.c. lattice with respect to the paracrystalline distortions. The best agreement within experimental error is found for the value

$$\frac{\beta^2}{\alpha^2+\beta^2}=0{\cdot}65\,.$$

Hence

$$\beta/\alpha=\sqrt{\frac{0{\cdot}65}{1-0{\cdot}65}}=1{\cdot}36 \qquad (8)$$

and we have fluctuations which are more sensitive to changes in direction than distance ('disc-like'). Outside the limits of experimental error a solution exists which is drawn on the left hand side of Fig. 8: a primitive cubic-lattice cell with $\beta^2 \ll \alpha^2$, and hence rod-like coordination statistics H_{100}, $H_{010} > H_{001}$.

In Table 3 the g_{hkl} values according to equation (3) and calculated from Fig. 8 are given for the reflexions 004, 022 and 111. In the fourth and fifth columns the g values and Δx_a values [*cf.* equation (3)] with respect to the conventional lattice constant $a=8{\cdot}53$ Å are given, showing that the smallest fluctuations are along the body diagonal. The sixth column gives the mean crystallite size in these directions. The value α^* is explained below. In Fig. 7 line widths are calculated for both cases (b.c.c. with $\beta/\alpha=1{\cdot}36$ and p.c. with $\beta/\alpha\sim 0$). Here again it is clearly seen that only a b.c.c. lattice is possible.

The question now arises: how long are the vectors of the coordination statistics along [111]? In another

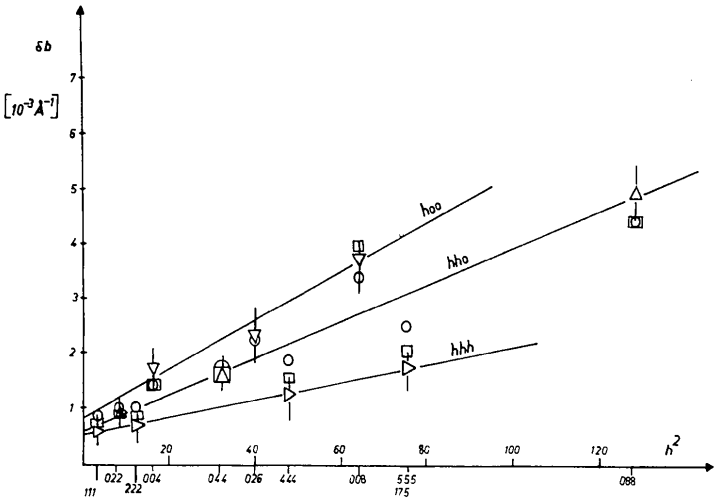

Fig. 7. Integral width, δb, *versus* h^2 of sample III. △ ▷ ▽ observed values; ○ calculated for a p.c. lattice, rod-like statistics; □ calculated for a b.c.c. lattice, sphere-like statistics.

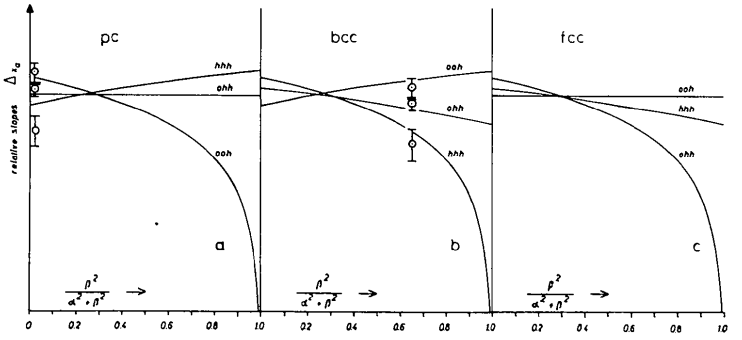

Fig. 8. Relative roots of the slopes Δx_a (logarithmic scale) of the *h*00, *hh*0, *hhh*, reflexions in the δb–h^2 plot for different Bravais lattices as a function of the relative shape $\beta^2/(\alpha^2+\beta^2)$ of the coordination statistics. ○ measured values of sample III.

paper (Hosemann, Lemm, Schönfeld & Wilke, 1967) a semi-empirical equation was discussed, which links the mean size L of a paracrystallite with its g value along the same direction:

$$L=d\left(\frac{\alpha^*}{g}\right)^2. \tag{9}$$

This equation was derived on the basis that in a paracrystalline lattice the standard fluctuation of the nth netplane is given by $\Delta x_n=\sqrt{n}\Delta x$; $\Delta x=gd$. If this fluctuation reaches the order of magnitude of a netplane distance d, the paracrystal can no longer increase in size. The empirical factor of proportionality was called α^*:

$$\Delta x_n=\sqrt{n}\,\Delta x\lesssim\alpha^* d\,. \tag{9a}$$

Hence equation (9). The quantity α^* is given by

$$\alpha^*=g\sqrt{\frac{L}{d}} \tag{10}$$

and can be calculated directly from the measurable quantities g, L and d. For many different solids we found $\alpha^*\simeq 0{\cdot}15$ (see Table 4).

If for instance H_{111} are coordination statistics at a distance $\bar{x}=\sqrt{3}a$ from the origin, we obtain from Table 3

$$\Delta x=31\times\sqrt[4]{3}=0{\cdot}040\text{ Å}\,,\quad g=0{\cdot}040/\sqrt{3}\times 8{\cdot}52=0{\cdot}0027$$

$$\alpha^*=0{\cdot}0027\sqrt{\frac{1700}{\sqrt{3}\times 8{\cdot}52}}=0{\cdot}029\,.$$

This value is about four times too small. If the coordination statistics are taken to be $H_{\frac{1}{4}\frac{1}{4}\frac{1}{4}}$, g and $\frac{1}{\sqrt{d}}$ both increase by a factor $\sqrt{4}$ and we obtain

$$\alpha^*\simeq 0{\cdot}12\,. \tag{11}$$

Since the coordination statistic is found in this way to be $H_{\frac{1}{4}\frac{1}{4}\frac{1}{4}}$, the physical significance of the model in Fig. 3 becomes apparent: the bricks of the spinel lattice are $\frac{a}{4}$-subcubes, which touch each other at the points $\frac{1}{4}\frac{1}{4}\frac{1}{4}$. If Mn^{3+} ions are built in on B sites (white circles in Fig. 3), the paracrystalline distortion is an expansion in the direction of the cube diagonals.

From the Δx_a value for [111] of Table 3 we calculate that the fluctuation of $H_{\frac{1}{4}\frac{1}{4}\frac{1}{4}}$ in the direction [111] and length $\frac{1}{4}\sqrt{3}$ is

$$\alpha=31\sqrt{\frac{1}{4}\sqrt{3}}=20{\cdot}4\text{ XU}. \tag{12}$$

The fluctuation perpendicular to it, assuming cylindrical symmetry, is then, according to (8)

$$\beta=1{\cdot}36\times 20{\cdot}4=28\text{ XU}\,. \tag{13}$$

6. Jahn–Teller microdomains

According to Table 2, sample I and the quenched sample II have small and almost no paracrystalline distor-

Table 4. *Equilibrium size and g values of the particles*

Samples	Lattice direction	a_k (Å)	L (Å)	g_a (%)	α^*
Polyethylene ultra-fibers in hot stretched samples	Normal to (110) plane	4·1	91 186	3·15 2·2	0·15 0·15
Polyethylene mosaic blocks in single crystals	Normal to (110) plane	4·1	332	2·14	0·19
Polyethylene mosaic-blocks in single crystals crystallized at higher temperatures	Normal to (110) plane	4·1	530	1·42	0·16
Al_2O_3-promoted α-Fe catalyst annealed 400 °C, 15 h	⟨001⟩ ⟨011⟩ ⟨111⟩	2·48	200 250 320	1·26 0·93 0·97	0·11 0·09 0·11
Al_2O_3-promoted α-Fe catalyst annealed 800 °C, 20 h	⟨001⟩ ⟨011⟩ ⟨111⟩	2·48	430 550 550	0·85 0·56 0·54	0·11 0·08 0·08
Al_2O_3-promoted α-Fe catalyst annealed 950 °C, 10 h	⟨001⟩ ⟨011⟩ ⟨111⟩	2·48	650 710 800	<0·1 <0·1 <0·1	0·16 0·17 0·18
Mn-rich cubic manganese ferrite	⟨001⟩ ⟨011⟩ ⟨111⟩	3·70	1150 1540 1740	0·62 0·54 0·36	0·15 0·16 0·12

* Here g_a is the relative fluctuation, reduced to the distance a
$g_a=\Delta x_a/a$.

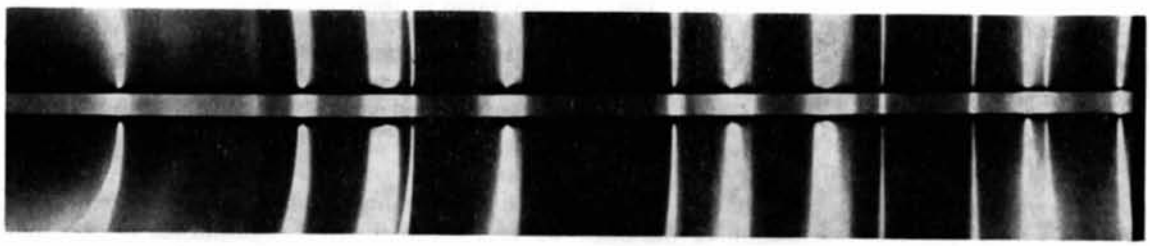

Fig. 9. Transmission pattern of sample III, heavily over exposed. Weak tetragonal 'feet' to the left and right of the main cubic lines are visible. Fe $K\alpha_1$, 50 kV, 7 mA, 90 h.

tions respectively. The line profiles are of the Lorentzian type –

$$\sim \frac{1}{1+(\gamma b)^2} .$$

We are concerned with almost undistorted cubic lattices. The situation is quite different for sample III cooled at a medium rate (Table 1). Fig. 9 is a superimposed X-ray-pattern, taken with Fe radiation.

One observes continuous blackening 'feet' with sharp edges on both sides of the pseudo-cubic Bragg reflexions. As can be seen from Fig. 10 the 'foot' length is greatest for reflexions near $h00$ and least for those close to the [hhh] direction. From the position of the foot edges (arrows in Fig. 11) one can calculate the lattice constants of the largely tetragonal deformed lattice cells. All reflexions give the same ratio $c/a=1{\cdot}056$, which agrees with the measured ratio of the macroscopic tetragonal (see again Fig. 11), slowly cooled specimen with $x=1{\cdot}88$ (see Fig. 1). Fig. 10 shows the good agreement between the values a_{max} and a_{min} calculated from the tetragonal structure and those calculated from the positions of the feet. Since these tetragonal feet also influence the integral widths of the reflexions, we measured only the half widths $\delta b_{1/2}$ of the central peaks. For a given profile function, which we assume to be equal for all reflexions, integral widths δb can be recalculated from the factor $\delta b : \delta b_{1/2}$. This factor has been determined as 1·75 from the 444 reflexion, which shows practically no tetragonal splitting and, hence no feet. The lines from the $x=1{\cdot}66$ sample are so sharp that their widths are practically equal to the collimation error; they are used for width correction of the $x=1{\cdot}88$ sample by linear substraction of the width, since the line profiles of both samples were nearly Cauchy-type in character, $f(b)=(1+k^2b^2)^{-1}$. Hence the widths of these profiles sum linearily (see the preceding paper).

The positions of the arrows of Fig. 11 were found visually, since according to the Mach phenomenon, the human eye can differentiate a photometercurve.

The central peaks in sample III prove that a cubic phase exists in addition to microdomains. Here no orientational correlation of the Jahn–Teller octahedra exists, or the domains are so small that their c/a values are nearly 1. We call the structure 'pseudo-cubic', since tetragonal microdomains are inbedded in a paracrystalline cubic matrix.

We shall now attempt to obtain quantitative information about these microdomains. Fig. 11 shows the microdensitometer curves of the 220 reflexion from samples III and IV. Obviously both curves possess an additional asymmetric intensity contribution. Moreover the curve of sample IV shows a weak hump between the main tetragonal reflexions 220 and 202 022, which corresponds to a small amount of the cubic phase. In Fig. 11 the curves are arranged to bring the cubic lines into coincidence on a vertical line.

(*a*) *Sample* III (*pseudocubic*)

If the tetragonal microdomains show no size broadening their intensity should exactly represent the frequency distribution of their c/a values. Moreover, these values should not excede the value $c/a=1{\cdot}056$ of sample IV. Moreover, the foot intensity of sample III spreads far beyond the point represented by this value (arrows in Fig. 11). This means that the real c/a-frequency distribution must be considerably smeared out by a microdomain-size distribution of very small domains.

We can therefore assume a relativly smooth pattern of microdomain intensity contributions, which will not affect the upper part of the central cubic peak. According to the theory for $\delta b \gtrsim 1{\cdot}5/L$ the central peak is closely represented by a Lorentzian profile produced by paracrystalline distortions. Now it is possible, by a simple geometric construction, to find the foot of the symmetrical central peak from the peak shape. The difference between this symmetrical part and the measured intensity has been included in Fig. 11. The proportion of the intensity below this curve, represented by the microdomains, is 26%.

(*b*) *Sample* IV (*pseudotetragonal*)

The reflexions of sample IV are divided according to the c/a value of the tetragonal phase. An additional contribution from microdomains with $c/a<1{\cdot}056$ is clearly visible in the overall profile (Fig. 11). Moreover, as already mentioned, there a small residual cubic hump can be seen. Obviously, here the matrix is tetragonal with $c/a=1{\cdot}056$. In this matrix microdomains, having other orientations, are present on clusters of

Jahn–Teller octahedra. The larger these microdomains are, the more their c/a value differs from 1·056. Such structures are called 'pseudotetragonal'.

In Fig. 12 the results of this section are illustrated schematically. The distribution of c/a values in the microdomains, which depends on the size distribution of these domains, is drawn as a step-function for convenience.

The separation of the three components, *i.e.* the contribution from the tetragonal matrix from that from the microdomains and the cubic phase can be simply achieved: the intensity difference between the tetragonal reflexions 220 and 202 022 has been reduced by the outer flanks of these reflexions, which are not much disturbed by a microdomain contribution. From the radius of curvature of the cubic-lattice hump we get a rough value for the cubic contribution. Thus we obtain:

Contribution of the tetragonal matrix	74%
tetragonal microdomains	23%
cubic phase	3–5%

7. Calculation of the paracrystalline distortion

We now try to calculate the observed g values from the same assumptions: in a tetragonal matrix with

$$c/a = 1+\varepsilon\,, \tag{14}$$

$100p$% of the B sites are occupied by Jahn–Teller octahedra with

$$\bar{c}/\bar{a} = 1+\bar{\epsilon} \tag{15}$$

as the average value.* In a cubic matrix $\varepsilon = 0$ and $\bar{\epsilon}$ lies between 0 and 0·056; in a tetragonal matrix $\varepsilon > 0$ and $\bar{\epsilon}$ is smaller the larger the microdomain. For very large domains $\bar{\epsilon}$ can be negative, if the c axis of such a domain is perpendicular to the c axis of the matrix.

In the first section of our calculation the B sites are randomly occupied by Mn^{3+} ions and clusters resulting from positional ordering do not occur. Domains of quite different sizes exist as a result of statistical fluctuation and their size distribution is given by a Boltzmann-statistic. The orientation of the c axes also is random. $p/3$ has a c axis parallel to the c axis of the incipient tetragonal matrix and $2p/3$ perpendicular to it.

Since according to Figs. 2 and 3 there is a B site every 8·53 Å ($=a$) along each cell edge, we propose that $(1-p)$ cell edges have length c in the direction [001] and a in the direction [010] and [100], $p/3$ cell edges have length $\bar{c}$ and $2p/3$ the length $\bar{a}$ statistically distributed in three cubic directions. Then the cell edge statistic consists of three parts:

$$\begin{aligned} H_{001} &= (1-p)H_m(x-c)+\tfrac{2}{3}p\,H_{\bar{a}}(x-a)+\tfrac{1}{3}p\,H_{\bar{a}}(x-\bar{c}) \\ H_{010} &= H_{100} \\ &= (1-p)H_m(x-a)+\tfrac{2}{3}p\,H_{\bar{a}}(x-\bar{a})+\tfrac{1}{3}p\,H_{\bar{a}}(x-\bar{c})\,. \end{aligned} \tag{16}$$

$H_m(x)$ is the distance statistic of the matrix and $H_{\bar{a}}(x)$ that of the microdomains, which for convenience can be replaced by point functions

$$P(x-c)\,,\quad P(x-a)\,,\quad P(x-\bar{a})\,,\quad P(x-\bar{c})\,.$$

Since according to Fig. 1 the volume of the matrix does not change at the transition point, we have

$$a_c^3 = a^2c = \bar{a}^2\bar{c}\,.$$

After substitution of (14) and (15) one obtains

$$\begin{aligned} \frac{a}{a_c} &= 1-\tfrac{1}{3}\varepsilon+\tfrac{2}{9}\varepsilon^2 & \frac{\bar{a}}{a_c} &= 1-\tfrac{1}{3}\bar{\epsilon}+\tfrac{2}{9}\bar{\epsilon}^2 \\ \frac{c}{a_c} &= 1+\tfrac{2}{3}\varepsilon-\tfrac{1}{9}\varepsilon^2 & \frac{\bar{c}}{a_c} &= 1+\tfrac{2}{3}\bar{\epsilon}-\tfrac{1}{9}\bar{\epsilon}^2\,. \end{aligned} \tag{17}$$

* The c/a value of an individual Jahn–Teller octahedra is naturally greater.

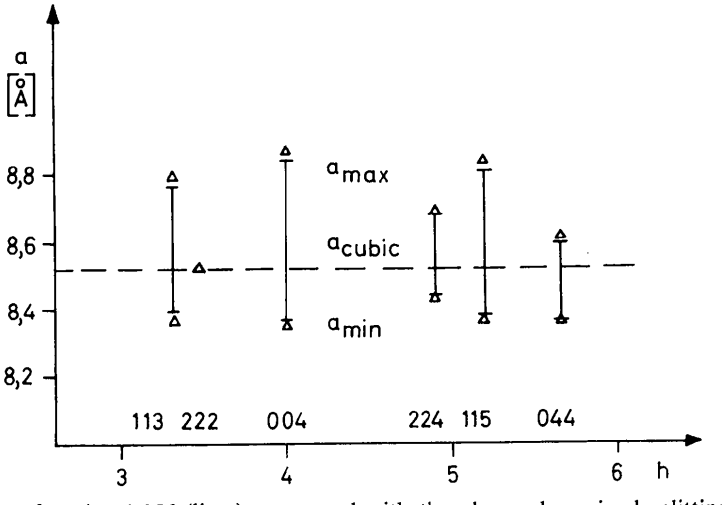

Fig. 10. Calculated line splitting for $c/a = 1{\cdot}056$ (lines), compared with the observed maximal splitting in Fig. 7 (triangles) for different reflexions.

Now we get from (16) and (17) directly

$$\begin{aligned}
\bar{x}_{001} &= (1-p)c + \tfrac{1}{3}p(2\bar{a}+\bar{c}) \\
&= a_c[1 + \tfrac{2}{3}\varepsilon(1-p) - \tfrac{1}{9}\varepsilon^2(1-p) + \frac{p}{9}\bar{\epsilon}^2], \\
\bar{x}^2_{001} &= a_c^2[1 + \tfrac{4}{3}\varepsilon(1-p) \\
&\quad + \varepsilon^2[\tfrac{4}{9}(1-p)^2 - \tfrac{2}{9}(1-p)] + \tfrac{2}{9}p\,\bar{\epsilon}^2], \\
\bar{x}^2_{001} &= (1-p)c^2 + \tfrac{1}{3}p(2\bar{a}^2+\bar{c}^2) \\
&= a_c^2[1 + \tfrac{4}{3}\varepsilon(1-p) + \tfrac{2}{9}(1-p)\varepsilon^2 + \tfrac{4}{9}p\,\bar{\epsilon}^2], \\
g^2{}_{001} &= \tfrac{2}{9}p[\bar{\epsilon}^2 + 2(1-p)\varepsilon^2]. \qquad (18)
\end{aligned}$$

In a similar way one obtains

$$\bar{x}_{010} = \bar{x}_{100} = a_c[1 - \tfrac{1}{3}\varepsilon(1-p) + \tfrac{2}{9}\varepsilon^2(1-p) + \frac{p}{9}\bar{\epsilon}^2]$$

$$g^2_{010} = g^2_{100} = \tfrac{2}{9}p[\bar{\epsilon}^2 + \tfrac{1}{2}(1-p)\,\varepsilon^2]. \qquad (19)$$

As can be seen from these equations, there is a small expansion in the [100] [010] direction and a small compression in the [001] direction of the tetragonal matrix, which thus tends towards cubic symmetry. The change in the lattice parameters is in the order of 1% however, and therefore not much greater than the accuracy to which the equilibrium lattice parameters are known.

For samples I, II and IV only the g_{111} values have been measured (Table 2). The g_{100} values necessary for comparison with equations (18) and (19) have been obtained by multiplying by the factor $g_{001}/g_{111} = (\frac{1}{2}1{\cdot}24)/0{\cdot}47 = 1{\cdot}32$ of sample III (Table 3) and are plotted in Table 5. This implies that the fundamental coordination statistics $H_{\pm\pm\pm}$ have not changed their shape in sample I, II or IV.

Sample I (*cubic*)

Since $\varepsilon = 0$, equations (18) (19) are identical. In § 4 we calculated g_{100} by neglecting any Jahn–Teller effect, *e.g.* $\bar{\epsilon} = 0$, but introducing the relative difference $\frac{dR}{R}$ of spherical ions. In equation (6) we obtained a value g_{100}, which within experimental error agrees with g_{111} of Table 2 after multiplication by the factor 1·32. Now introducing the Jahn–Teller effect we obtain from equations (18) and (19) a further correction,

$$g_{001} = g_{100} = \tfrac{1}{3}\sqrt{2p}\,\bar{\epsilon}, \qquad (20)$$

which must be small enough compared with the observed value 0·13% of Table 5. Hence

$$\bar{\epsilon} \lesssim 0{\cdot}05.$$

In sample I with $p = 0{\cdot}33$ (Table 1) such a small Jahn–Teller effect is possible. This agrees with the results of Červinka (1965) who found anomalously large Debye factors which he explained by tetragonal deformation of individual single octahedra on *B* sites.

Sample II (*cubic*)

The observed g_{100} value is so large compared with sample I, that the volume effect of equation (6) can be

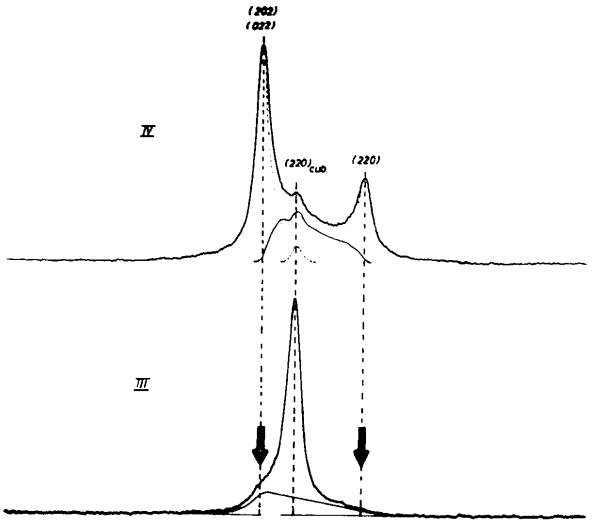

Fig. 11. Line profiles of the reflexion 220 of samples III and IV brought to the same horizontal scale. The arrows indicate the end of the feet, visually observed (Mach phenomenon). They fit nicely with the lines of the tetragonal matrix of sample IV.

SAMPLE N°	STRUCTURE macroscopic	CORRELATION OF $MnO_6^{3-\,2-}$ positional (clusters)	CORRELATION OF $MnO_6^{3-\,2-}$ orientational (microdomains)	X-RAY pattern	DISTRIBUTION of c/a - values in the crystal
II	cubic	no	no	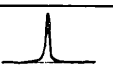	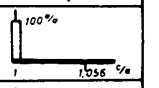
III	pseudocubic	yes	yes	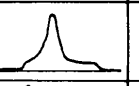	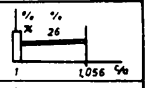
IV	pseudotetragonal	yes	yes		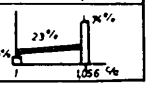

Fig. 12. Line profiles and distribution of *c*/*a* in the microdomains and matrices (schematic). An orientational correlation is proved by the experiments; a positional correlation cannot be excluded, but is unlikely.

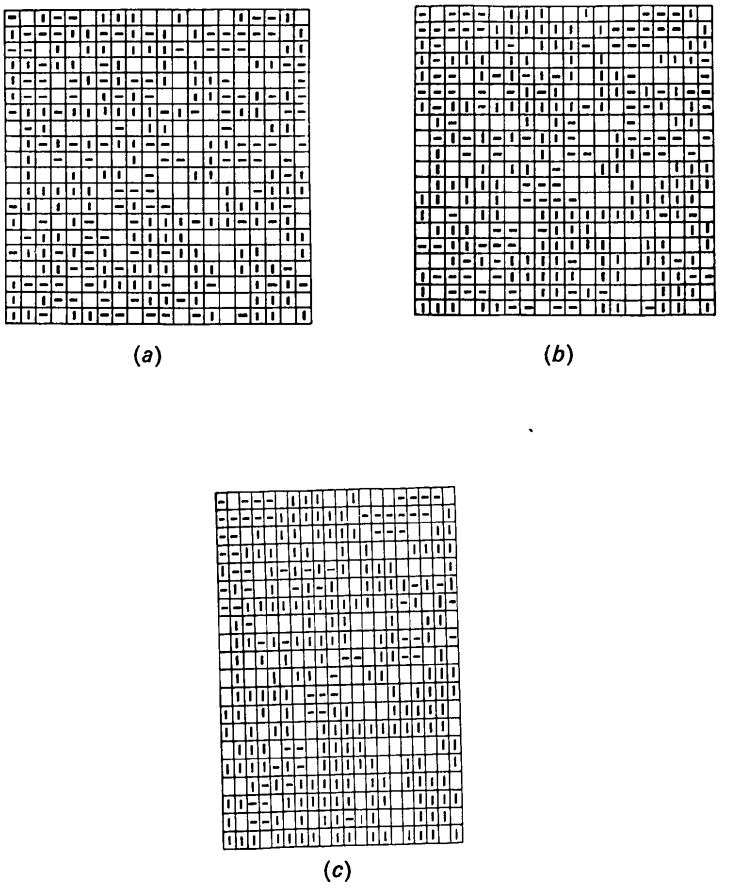

Fig. 13. Two-dimensional models of samples II–IV. See Table 6 for details.

ignored. For $\varepsilon=0$ equations (17) and (19) degenerate to equation (20). For $p=0{\cdot}44$ and g_{obs} we obtain $\bar{\epsilon}=0{\cdot}014$. As mentioned above, this is a value averaged over a distribution ranging from $\bar{\epsilon}=0$ (for very small microdomains) to $\bar{\epsilon}=0{\cdot}056$ (for very large microdomains). The mean tetragonality of the microdomains in the cubic sample II $\varepsilon=0{\cdot}014$, which is much smaller than the limiting value $\varepsilon=0{\cdot}056$. This is evidence for the smallness of the domains. More information can not be obtained from the X-ray pattern, since the reflexions have a poor Lorentzian profile (Fig. 11).

Sample III (*pseudocubic*)

Within our simplified model we will make use of the $\bar{\epsilon}$ value of sample II for sample III. However, the observed microdomains must be taken into account. A rough attempt to do this is made by introducing the following simple assumption of correlation: all the distorted octahedra must occur in parallel oriented pairs, as in the undistorted case. Then all the above equations hold, if we put $c \to 2c$, $a \to 2a$, $\bar{a} \to 2\bar{a}$, $\bar{c} \to 2\bar{c}$, $g_{100} \to g_{200}$. This means that we obtain the same g value for the second neighbours as for sample II. Then according to equation (9*a*) the g_{100} value for first neighbours increases by the factor $\sqrt{2}$.

As can be seen from Table 5 the observed value g_{100} now fits with the calculated one. The correlation factor γ, in this case 2, has the physical meaning that orientational and positional correlations exist here between next-neighbour Mn^{3+} ions (Fig. 13). The statistical domains of parallel oriented Mn^{3+} ions are now systematically twice as large as in sample II.

Another extreme explanation is given on the right hand side of Table 5. Instead of enlarging γ by the factor 2 the mean tetragonality can be enlarged by the factor $\sqrt{2}$. Since with increasing γ the mean tetragonality $\bar{\epsilon}$ also increases, the most probable solution is to be expected between the two limiting cases of Table 5, for instance

$$\gamma \sim 1{\cdot}6\,; \quad \bar{\epsilon}=0{\cdot}016\,.$$

The microdomains produced by the orientational and positional correlation determine the size of the feet of the reflexions (Figs. 11 and 12). As shown in § 6*a* and Fig. 12, approximately 26% of the *B* sites belong to such tetragonal microdomains.

Sample IV (*pseudotetragonal*)

Since the ε value of the matrix is not zero, because of equations (18) and (19), there exist different g values in different axial directions. Only one mean $\bar{g}_{100}$ value is available from experiments. Therefore we must compare the mean g value of equations (18) and (19):

$$\tfrac{1}{3}(g_{100}^2+g_{010}^2+g_{001}^2)=\bar{g}_{100}^2=\tfrac{2}{9}p[\bar{\epsilon}^2+(1-p)\,\varepsilon^2]\,. \quad (22)$$

Herefrom we obtain a g value of 1·39% which is to high compared with that observed (Table 5). Taking into account that according to § 6*b* and Fig. 12 only 23% of the B sites belong to the microdomains, *i.e.*

$$p=0{\cdot}23\,, \quad (23)$$

we obtain a g value $g=1{\cdot}16$ which is in better agreement with the observed value.

8. Three models illustrating the cubic-tetragonal phase transition

The models (Fig. 13) were constructed by means of dice: 1 and 0 points, no Mn^{3+}-occupied octahedra; 3 and 4 points, Mn^{3+}-occupied octahedra with the c axis horizontal; 5 and 6 points, M^{3+}-occupied octahedra with the c axis vertical. Hence $p=\frac{2}{3}$ in this two-dimensional structure.

Sample II is represented by Fig. 13(*a*): no positional or orientational correlation. Nevertheless, statistically, microdomains exist up to 10 parallel-oriented Jahn–Teller ions. In Table 6 the distribution of the different B sites is given.

In Fig. 13(*b*) the structure of Fig. 13(*a*) is changed as follows:

Jahn–Teller-octahedra, which have 4, 3, 2,
direct (100)-neighbours, change their orientation if at least..... 3, 2, 2,
neighbours have another orientation.

According to Table 6 168 octahedra now have a vertical orientation and build up much larger microdomains with orientational correlation. Since, according to Table 3, the paracrystalline lattices have average diameters of 1740 Å, each microcrystal contains so many microdomains that a preferred orientation can not, as yet, be found. The lattice still remains pseudocubic.

In Fig. 13(*c*) the structure of Fig. 13(*b*) is changed as follows:

The c axis of Jahn–Teller-octahedra, which have..... 4 3 2 1
direct (100)-neighbours, change their vertical orientation, if at least..... 3 2 2 1
neighbours have a horizontal orientation, and change their horizontal orientation, if at least..... 2 2 1 1
neighbours have a vertical orientation.
(This process was repeated twice.)

Here the transition to the vertical orientation is favoured since in Fig. 13(*b*) this orientation was predominant outside statistical fluctuation (Table 6). The matrix now becomes tetragonal. Only relatively small domains of cross orientation exist, (in sample IV they exist to the extent of $p=0{\cdot}23$ [see equation (23)]. In Fig. 13(*c*) this proportion is large ($p=0{\cdot}14$). Apparently the stress in the matrix gives rise to a tetragonality $\bar{\epsilon}>0$, though their c axes are perpendicular. Only very large domains then have $\bar{\epsilon}<0$. In the calculation of the last model of Table 5 we found $\bar{\epsilon}=0{\cdot}014\sim\frac{1}{4}\varepsilon$.

References

BLASSE, G. (1965). *Philips Res. Reports*, **20**, 528.
ČERVINKA, L. (1965). *J. Phys. Chem. Solids*, **26**, 1917.
ČERVINKA, L. (1966). Dissertation (Institute of Solid State Physics) Czechoslovak Academy of Science, Prague.
ČERVINKA, L., KRUPIČKA, S. & SYNEČEK, V. (1961). *J. Phys. Chem. Solids*, **20**, 167.
ČERVINKA, L. & VETTERKIND, D. (1968). *J. Phys. Chem. Solids*, **29**, 171.
FINCH, G. F., SINHA, A. P. B. & SINHA, K. P. (1957). *Proc. Roy. Soc.* A **242**, 28.
GOODENOUGH, J. B. (1965). *J. Appl. Phys.* **36**, 2342.

Table 5. *Calculation of* g_{100} *values*

Sample	g_{100} observed	g_{100} calculated	Tetragonality ε	Tetragonality $\bar{\epsilon}$	Correlation factor, γ	Alternative solution $\bar{\epsilon}$	Alternative solution γ	p
I	<0·13%	0·16%	0	<0·005	1	>0	–	
II	0·43	0·43	0	0·014	1	–	–	
III	0·62	0·61	0	0·014	2	0·02	1	0·44
IV	0·96	1·39	0·056	0·014	1	–	–	–
	0·91	1·16	0·056		–	0·014	1	0·23

Table 6. *Distribution of* Mn^{3+} *ions in* Fig. 13

Fig.	Sample	No.	Jahn–Teller ion on a B site: Axis horizontal	Jahn–Teller ion on a B site: Axis vertical	Correlations: Positional	Correlations: Orientational
(*a*)	II	124	121	155	No	No
(*b*)	III	124	108	168	No	Yes
(*c*)	IV	124	67	209	No	Yes

GOODENOUGH, J. B. (1967). Private communication.
HOFFMANN, E. G. & JAGODZINSKI, H. (1955). *Z. Metallkunde*, **46**, 611.
HOSEMANN, R., BIALAS, D., SCHÖNFELD, A., WILKE, W. & WEICK, D. (1966). *Advances in Materials*. Oxford: Pergamon Press.
HOSEMANN, R., LEMM, K., SCHÖNFELD, A. & WILKE, W. (1967). *Kolloid-Z., Z. Polymere*, **216**, 103.
JAHN, H. A. & TELLER, E. (1937). *Proc. Roy. Soc.* A**161**, 220.
MCMURDIE, H. F., SULLIVAN, B. M. & MAURER, F. A. (1950). *J. Res. Nat. Bur. Stand.* **45**, 35.
ROGERS, D. B., GERMANN, R. W. & ARNOTT, R. J. (1965) *J. Appl. Phys.* **36**, 2338.
ŠIMŠA, Z. (1967). *J. Phys. Chem. Solids*, **28**, 2435.
VOGEL, W. & HOSEMANN, R. (1970). *Acta Cryst.* A**25**, 272.
WICKHAM, D. G. & CROFT, W. J. (1958). *J. Phys. Chem. Solids*, **7**, 351.
WOJTOWICZ, P. J. (1959). *Phys. Rev.* **116**, 32.

Acta Cryst. (1970). A**26**, 289

Rigid-Body Molecular Motion in Crystals. The Centre of Libration

BY G. S. PAWLEY*

Department of Natural Philosophy, Edinburgh University, Drummond Street, Edinburgh 8, *Scotland*

(*Received* 17 *June* 1969 *and in revised form* 27 *October* 1969)

It is shown that the concept of the molecular centre of libration in the description of the average rigid-body thermal behaviour of molecules is a useful approximation. A restriction is made on the full theory, making the centre of libration model a constrained version of the complete model. The relationship between the models is discussed. Some examples are chosen to demonstrate the closeness of the approximation. These results show that for data reaching a reliability factor of no better than 7% an analysis using the full theory might yield a meaningless result. Some data of much higher accuracy does, however, show the need for the full theory.

Introduction

In a recent paper Schomaker & Trueblood (1968) show that the correct description of the average motion of rigid molecules in a crystal is furnished by a model with 20 parameters. These determine the mean-square translational and librational tensors **T** and **L**, each with six independent coefficients, and the screw rotation tensor **S** with eight independent coefficients. Throughout the present paper this will be called the TLS model. Before this theory was developed a model with 15 parameters had been used by Hirshfeld, Sandler & Schmidt (1963), Pawley (1963) and Cruickshank, Jones & Walker (1964). To the twelve coefficients of **T** and **L** were added three coordinates for the centre of molecular libration **X**. This will be called the TLX model.

The TLX model has proved most successful, especially when applied during structure factor least-squares (SFLS) refinement (Pawley, 1966). This procedure requires a constrained SFLS refinement, resulting in rigid-body parameters giving the best least-squares fit to the diffraction data. The alternative procedure is to perform the standard SFLS refinement, and then fit the model to the independent atomic vibration tensors $\mathbf{U}_x$ thus found. The fit by this method cannot be the better; for anthracene the least-squares errors from this procedure were almost twice those obtained from the constrained SFLS refinement (Pawley, 1967). Another constrained SFLS program is therefore called for to test the data available in the literature to find examples where the TLS model provides a significant improvement over the TLX model. First let us establish the relationship between the TLS and the TLX models and find the transformation equations governing this relationship.

* Present address: Chemistry Department, The University of Århus, Denmark.

The TLX and TLS models

Let us examine the equations relating the $\mathbf{U}_x$ for the atom at the point **x** in a molecule to the three tensors **T**, **L** and **S**. These are given by Pawley (1968) equations (3):

$$(\mathbf{U}_x)_{11} = T_{11} + L_{22}x_3^2 + L_{33}x_2^2 - 2L_{23}x_2x_3 + 2S_{21}x_3 - 2S_{31}x_2$$
$$(\mathbf{U}_x)_{23} = T_{23} + L_{31}x_1x_2 + L_{12}x_3x_1 - L_{23}x_1^2 - L_{11}x_2x_3 + S_{33}x_1 - S_{13}x_3 + S_{12}x_2 - S_{22}x_1 \,. \quad (1)$$

We must now compare these with the equations relating the $\mathbf{U}_x$ to the two tensors **T** and **L** and the molecular centre of libration **X**. These can be obtained from the